Formation and Thermal Stability of Au₂O₃ on Gold Nanoparticles: Size and Support Effects

Luis K. Ono and Beatriz Roldan Cuenya*

Department of Physics, University of Central Florida, Orlando, Florida 32816

Received: November 28, 2007; In Final Form: January 9, 2008

Gold nanoparticles with two different size distributions (average sizes of ~1.5 and ~5 nm) have been synthesized by inverse micelle encapsulation and deposited on reducible (TiO_2) and nonreducible (SiO_2) supports. The thermal and chemical stability of oxidized gold species formed upon cluster exposure to atomic oxygen have been investigated in ultrahigh vacuum using a combination of temperature-, time- and CO dosing-dependent X-ray photoelectron spectroscopy (XPS), as well as temperature-programmed desorption (TPD). Our work demonstrates that (a) low-temperature (150 K) exposure to atomic oxygen leads to the formation of surface as well as subsurface gold oxide on Au nanoparticles, (b) the presence of the reducible TiO_2 substrate leads to a lower gold oxide stability compared to that on SiO_2, possibly because of a TiO_2 oxygen vacancy-mediated decomposition process, (c) heating to 550 K (Au/SiO_2) and 300 K (Au/TiO_2) leads to a near-complete reduction of small (~1.5 nm) NPs while a partial reduction is observed for larger clusters (~5 nm), and (d) the desorption temperature of O_2 from preoxidized Au clusters deposited on SiO_2 depends on the cluster size, with smaller clusters showing stronger O_2 binding.

Introduction

Bulk gold is known as one of the most inert metals in the periodic table.[1] This trait is attributed to the lack of interaction between the orbitals of adsorbates and the filled *d* states of gold.[2,3] The high value of the enthalpy of oxygen chemisorption by gold to form its oxide Au_2O_3 ($\Delta H = +19.3$ kJ/mol) also indicates its chemical inertness.[4] However, pioneering work by Haruta et al. has demonstrated that highly dispersed Au nanoparticles (NPs) (<10 nm) supported on TiO_2 are considerably active for the low-temperature oxidation of CO[5] and C_3H_6 epoxidation.[6] Since then, the topic of gold in catalysis has received significant attention. Despite the large number of reports currently available, the microscopic origin of gold's heterogeneous catalytic activity is still poorly understood, and lack of consensus prevails with respect to the nature of the active sites,[7−9] the chemical state of the active gold species (metallic vs ionic gold),[10−12] as well as the relative importance of the different oxygen species (chemisorbed oxygen, surface oxide, subsurface oxygen) that might be present on these catalysts under realistic reaction conditions.[13,14]

Several authors attribute the enhanced chemical reactivity of gold NPs to the presence of ionic gold; however, whether anionic or cationic ($Au^{\delta-}$, $Au^{\delta+}$) gold species are preferable is still a matter of debate.[11,12,14−17] The presence of cationic interfacial gold species has been inferred on catalytically active systems such as Au deposited on reduced TiO_2.[18] This is contrary to the traditional picture involving electron transfer from oxide supports to Au NPs. Positively charged atoms at the metal−support interface have been observed, and their presence has been correlated to the enhanced catalytic activity of the system.[19,20] The active role of these cationic gold species on the water−gas shift reaction (WGS) has been demonstrated recently by Fu et al.[21] In that work, similar activities for the

WGS reaction were obtained on gold NPs supported on La-doped CeO_2 before and after the removal of the metallic gold species.[21] This result suggested a strong interaction of ionic gold with the ceria support, and the authors claimed that the presence of metallic NPs was not necessary for this catalytic reaction.[22]

On the theoretical side, several density functional theory (DFT) works have investigated the strength of the binding of CO,[23,24] O_2,[25,26] propene,[27] and methanol[28] to nonmetallic Au clusters. Here, a common trend was found, with reactant molecules showing stronger binding energy to anionic and cationic gold species, as compared to metallic gold. Recent hybrid DFT calculations carried out by Okumura et al.[9] suggested that although O_2 activation occurs on anionic Au cationic Au atoms show stronger bonding to CO. The authors proposed a model of dynamic charge polarization in which a strong heterojunction between Au clusters and their support is indispensable for the activation of oxygen species. The presence of negatively charged atoms in the perimeter region of Au NPs was attributed to localized Coulomb blockade effects. Furthermore, this surface negative charge was found to increase with decreasing cluster size,[29] in agreement with the known enhanced catalytic activity observed for small Au clusters.

Several experimental studies have been dedicated to the electronic and chemical characterization of oxidized gold species on Au single crystals,[30−32] polycrystalline films,[33,34] and the surface of Au NPs.[35,36] The instability of Au_2O_3 formed upon exposing a gold film (100 nm) to O_2 plasma has been reported by Tsai et al.[37] In this work, an activation energy of 57 kJ/mol was extracted for the decomposition of gold oxide from the correlation of electrical resistance measurements, conducted in air at room temperature (RT), and X-ray photoelectron spectroscopy (XPS) investigations after several time intervals. A nonmonotonic interaction of size-selected gold clusters with atomic oxygen was found by Boyen et al.[35] More specifically, 1.4 nm clusters (55 atoms, closed-shell electronic structure) were found to be resistant to oxidation. However, when larger (>1.6

* To whom correspondence should be addressed. E-mail: roldan@physics.ucf.edu.

TABLE 1: Summary of the Parameters Tuned and Average Height and Diameter of Au Nanoparticles Deposited on SiO$_2$ and TiO$_2$

sample	substrate	PS/P2VP molecular weight (g/mol)	HAuCl$_4$/ P2VP ratio	height (nm)	diameter (nm)	interparticle distance (nm)
no. 1	SiO$_2$	53 000/43 800	0.4	4.9 ± 1.6	16 ± 3	50 ± 6
no. 2	TiO$_2$	53 000/43 800	0.4	5.4 ± 1.2	19 ± 5	51 ± 18
no. 3	SiO$_2$	8200/8300	0.05	1.7 ± 0.8	12 ± 4	24 ± 4
no. 4	TiO$_2$	8200/8300	0.05	1.4 ± 0.5	10 ± 4	59 ± 40

nm) and smaller clusters (<1.3 nm) were exposed to an identical treatment, Au(core)/Au$_2$O$_3$(shell) structures with oxide shell thicknesses on the order of 0.7 nm were obtained.

Recently, a number of experimental studies discussing the chemical reactivity of gold surfaces precovered with atomic oxygen have been published.[38−41] Min et al.[42] reported the existence of three types of oxygen species on Au(111): (i) chemisorbed oxygen (oxygen bound to gold that is not part of an ordered phase), (ii) oxygen in surface oxide (well-ordered two-dimensional phase), and (iii) subsurface oxygen or bulk oxide (three-dimensional phase). On the basis of CO oxidation studies, the authors found the following relation among the reactivity of the different oxygen species: chemisorbed oxygen > oxygen in surface oxide > oxygen in bulk gold oxide.[42] The role played by these species in the thermodynamics and kinetics of oxidation/reduction reactions is a major challenge for the microscopic understanding of gold catalysis. This understanding becomes highly challenging when small NPs are considered because of the added complexity of the presence of different facets, kinks, and steps[43] and substantial interactions with the support.[44] As an example, on ~6 nm Au NPs deposited on highly ordered pyrolytic graphite (HOPG), Lim et al.[36] observed by XPS the formation of a single oxygen species upon exposure to atomic oxygen under ultrahigh-vacuum (UHV) conditions. This species was ascribed to chemisorbed oxygen because it was found to readily react with CO producing CO$_2$. Interestingly, two different oxygen species were identified on similarly treated but smaller gold NPs (~3 nm). In this case, one of the oxygen species was assigned to chemisorbed oxygen, which decomposes rapidly upon CO exposure, and the other to subsurface oxygen, inert toward reaction with CO.

Our work intends to address the following questions: (1) under which conditions is gold oxide stable on a gold nanoparticle, (2) how are the chemical kinetics of gold oxide decomposition affected by the size of the particles and the nature of their metal oxide support, and (3) is more than one gold oxide species (surface and subsurface) stable on NPs? In order to gain insight into these topics, we have used micelle encapsulation methods[43−48] to synthesize size- and shape-selected gold nanoclusters supported on thin SiO$_2$ and TiO$_2$ films. Morphological characterization was conducted by atomic force microscopy (AFM), and the decomposition of oxidized gold species, formed upon in situ O$_2$ plasma exposure, was investigated in UHV by XPS. Temperature-programmed desorption (TPD) measurements provided information on the reaction order and activation energy for molecular oxygen desorption from Au$_2$O$_3$(shell)/Au(core) NPs supported on SiO$_2$. Finally, CO exposure experiments were conducted to distinguish surface oxides from subsurface oxides.

Experimental Section

Size-selected Au nanoparticles were synthesized by inverse micelle encapsulation on polystyrene-block-poly(2-vinylpyridine) diblock copolymers [PS(x)-b-P2VP(y), Polymer Source Inc.]. When the PS-P2VP polymers are dissolved in toluene, inverse micelles are formed with the polar units (P2VP) constituting the core and the nonpolar polystyrene (PS) tails

extending outward. Subsequently, chloroauric acid (HAuCl$_4$· 3H$_2$O) is added to the polymeric solution and AuCl$_4^-$ compounds attach to the pyridine groups in the P2VP core. The micelles containing Au NPs are deposited onto different substrates by dip-coating at a speed of 1 μm/min. The NP size can be tuned by changing the molecular weight of the polymer head (P2VP) as well as the metal salt/P2VP concentration ratio. The length of the polymer tail (PS) determines the interparticle distance. In this study, the following two polymers have been used: PS(53000)−P2VP(43800) and PS(8200)−P2VP(8300). Naturally oxidized Si(111) wafers and ultrathin Ti films (15 nm) electron-beam deposited on Si(111) have been used as NP supports. Further details on this preparation method can be found in refs 43−48. A summary of the synthesis parameters used is given in Table 1.

The characterization of the sample morphology was performed ex situ by AFM in tapping-mode (Digital Instruments, Multimode). The ex situ prepared samples were mounted on a molybdenum sample holder with a K-type thermocouple located directly underneath the sample and transferred into a modular UHV system (SPECS GmbH) for polymer removal and electronic/chemical characterization. The system is equipped with an hemispherical electron energy analyzer (Phoibos 100, SPECS GmbH) and a dual-anode (Al Kα, 1486.6 eV and Ag Lα, 2984.4 eV) monochromatic X-ray source (XR50M, SPECS GmbH) for XPS, and a differentially pumped quadrupole mass spectrometer (QMS, Hiden Analytical, HAL 301/3F) with an electron-beam sample heating system connected to a PID temperature controller (Eurotherm, 2048) for TPD experiments. The base pressure in this chamber is $1-2 \times 10^{-10}$ mbar.

Polymer removal from the Au NP's surface was conducted by O$_2$ plasma exposure (Oxford Scientific, OSMiPlas) at low temperature (150 K) at a pressure of 5.5×10^{-5} mbar for 100 min. The polymer is removed during the first 20−30 min of this treatment, and further O$_2$ plasma exposure results in the formation of Au−O compounds. The XPS measurements, conducted immediately after the O$_2$ plasma treatments, were done with the sample at a temperature lower than 200 K. For the temperature-dependent decomposition of gold oxide (XPS), a linear heating ramp with $\beta = 3$ K/s was used. Because all of our annealing treatments were conducted in vacuum, lower decomposition temperatures for gold oxide are expected in our case as compared to similar studies conducted under higher partial O$_2$ pressure.[37]

The XPS binding energy (BE) scale has been calibrated using the Ti-2p$_{3/2}$ peak on Ti (454.2 eV) and Si-2p$_{3/2}$ peak on Si (99.3 eV) substrates as references. We can see the Ti^0 and Si^0 peaks because of the ultrathin nature of our TiO$_2$ [TiO$_2$(6 nm)/Ti(9 nm)/SiO$_2$/Si(111)] and SiO$_2$ [SiO$_2$(4 nm)/Si(111)] support films. From cross-sectional TEM measurements (not shown), the thicknesses of the TiO$_2$ and SiO$_2$ films are 6.0 ± 0.5 and 3.8 ± 0.5 nm, respectively. Because Au$_2$O$_3$ is known to decompose under intense X-ray exposure within hours,[31] a control experiment was conducted to ensure that no gold oxide decomposition occurred during our XPS acquisition time (~10 min). A maximum decrease in the Au^{3+} signal of 2% was observed under

our measurement conditions (Al Kα radiation, 1486.6 eV at a power of 300 W). For the analysis of peak positions, line widths, and relative areas of the Au^0 and Au^{3+} components, the raw XPS spectra were fitted with two (Au^0) or four (Au^0, Au^{3+}) Gaussian functions after linear background subtraction. During the fitting, the intensity ratio between the $Au-4f_{7/2}$ and $Au-4f_{5/2}$ peaks was fixed to 0.75, and the full width at half-maximum (fwhm) of the different components was 1.3 ± 0.3 eV (Au^0) and 1.7 ± 0.5 eV (Au^{3+}).[34]

Prior to the TPD measurements, the polymer-free Au NPs were flash-annealed to 700 K. This procedure reduced the residual gas background significantly at high temperatures without inducing any significant changes in the NP size distribution. Subsequently, the samples were exposed to atomic oxygen at a pressure of 2.3×10^{-5} mbar for 15 min. For the TPD studies, the samples were kept at RT during O_2 plasma exposure because a cold plasma treatment resulted in an increase of the background of the TPD spectra. Subsequently, the samples were placed ~3 mm away from the mass spectrometer glass shield opening (5 mm aperture) and heated at a rate of 5 K/s.

In order to investigate if for a given particle size and support combination, both surface and subsurface gold oxide species were formed upon exposure to atomic oxygen at low temperature (150 K), the samples were dosed with CO ($P_{CO} = 1.0 \times 10^{-5}$ mbar for 10 min, 4500 L), and the Au^{3+} XPS signal was monitored before and after CO exposure. All samples were dosed with CO at RT except sample no. 4, for which the CO dosing was conducted at ~150 K (and XPS measured at ~200 K) in order to prevent significant thermal decomposition of the relatively unstable oxide formed on this sample.

Results and Discussion

(a) Morphological Characterization (AFM). Figure 1 displays AFM micrographs of Au NPs with two different size distributions synthesized using diblock copolymers with different molecular weights: PS(53000)−P2VP(43800) (Figure 1a−d), and PS(8200)−P2VP(8300) (Figure 1e and f). The particles were deposited on SiO_2, Figure 1a and e (samples 1 and 3) and on TiO_2, Figure 1c and f (samples 2 and 4), and all images were taken after polymer removal using O_2 plasma. In addition, the influence of annealing in UHV to 700 K (sample no. 1) and 500 K (sample no. 2) on the nanoparticle size was monitored, Figure 1b and d, respectively. No significant size changes were observed in any of the samples upon annealing. The sizes of the Au NPs estimated by AFM after O_2 plasma are given in Table 1. Particles with similar size distributions (4.9−5.4 nm height for samples 1 and 2, and 1.4−1.7 nm for samples 3 and 4) were found on both substrates when the same encapsulating polymer was used in the synthesis. Because of the AFM tip-convolution effects (tip radius < 7 nm), the average NP height was used as the characteristic size parameter.

(b) Electronic Characterization (XPS). The thermal decomposition of oxidized gold species in core(Au^0)/shell(Au^{3+}) nanoparticles was monitored in situ (UHV) by XPS. Figure 2 shows XPS spectra from the Au-4f core level region of our four samples as a function of the annealing temperature. Spectra (i) were measured at ~200 K directly after a low-temperature (~150 K) O_2 plasma treatment. Spectra ii and iii were acquired after isothermal sample annealing for 10 min at 400 and 500 K respectively, followed by a fast cool down to room temperature using liquid nitrogen flow. The two doublets observed with maxima at (84.6 ± 0.3, 88.4 ± 0.3 eV) and (86.9 ± 0.2, 90.6 ± 0.2 eV) were assigned to the $4f_{7/2}$ and $4f_{5/2}$ core levels of Au^0 and Au^{3+} in Au_2O_3.[35,36,44] The vertical reference lines in
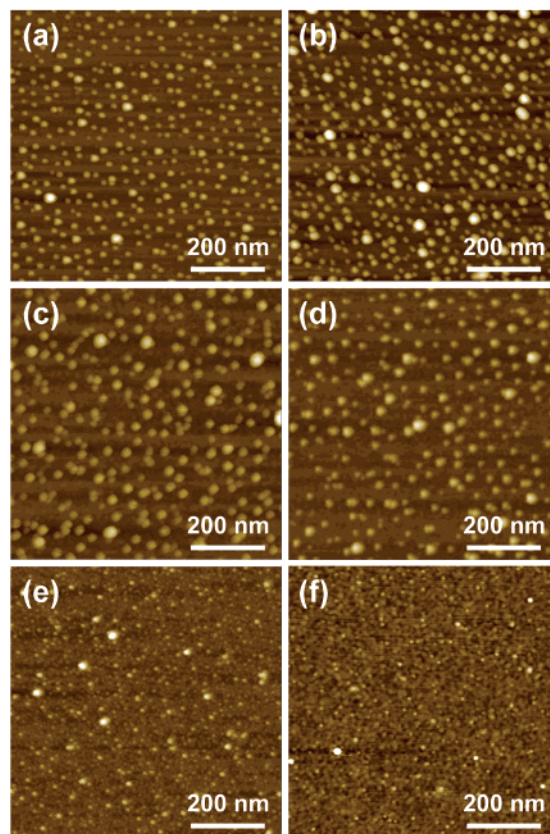

Figure 1. Tapping-mode AFM images of size-selected Au nanoparticles supported on SiO_2 [samples 1 (a) and 3 (e)] and on TiO_2 [samples 2 (c) and 4 (f)] taken after an in situ O_2 plasma treatment (90 W, 5.5×10^{-5} mbar, 100 min) at 150 K. The images shown in b and d correspond to samples 1 and 2 after a subsequent flash anneal in UHV at 700 K (b) and 500 K (d), respectively. The particles were synthesized by encapsulation in two different diblock copolymers: PS(53000)−P2VP(43800) (samples 1 and 2) and PS(8200)−P2VP(8300) (samples 3 and 4). The height scales are (a) $z = 20$ nm, (b) $z = 20$ nm, (c) $z = 30$ nm, (d) $z = 30$ nm, (e) $z = 12$ nm, and (f) $z = 8$ nm.

Figure 2 indicate the binding energies of bulk metallic gold (84.0 and 87.7 eV, solid lines) and Au^{3+} (85.8 and 89.5 eV, dashed lines).[34,49] The different Au−O species cannot be distinguished based on XPS spectra from the Au-4f region. Previous studies by Friend's group[42] on preoxidized gold single crystals demonstrated the presence of distinct Au−O species (chemisorbed oxygen, surface, and bulk gold oxide) based on the appearance of multiple peaks in their O-1s XPS spectra. A similar analysis of our samples is more difficult because our substrates (SiO_2 and TiO_2) already contain oxygen and the overlap between the binding energies of the different oxide species makes their individual detection challenging.

In Figure 2, positive shifts in BE were observed, and in agreement with previous literature reports,[43,44,50] their magnitude was found to strongly depend on the size of the NPs and the nature of the substrate. In particular, BE shifts of $+0.3 \pm 0.1$ eV (sample no. 1), $+0.2 \pm 0.1$ eV (sample no. 2), $+0.9 \pm 0.1$ eV (sample no. 3), and $+0.8 \pm 0.1$ eV (sample no. 4) were measured on our samples after annealing at 350 K. By comparing the BE values of samples with two distinct size distributions, deposited on the same substrate (SiO_2), a clear size effect is observed with the smallest particles (1.7 nm, sample no. 3) displaying larger BE shifts (+0.6 eV) than the 4.9 nm clusters in sample no. 1. The same conclusion is true when differently sized clusters are deposited on TiO_2 (samples 2 and 4). Positive BE shifts observed for small clusters are
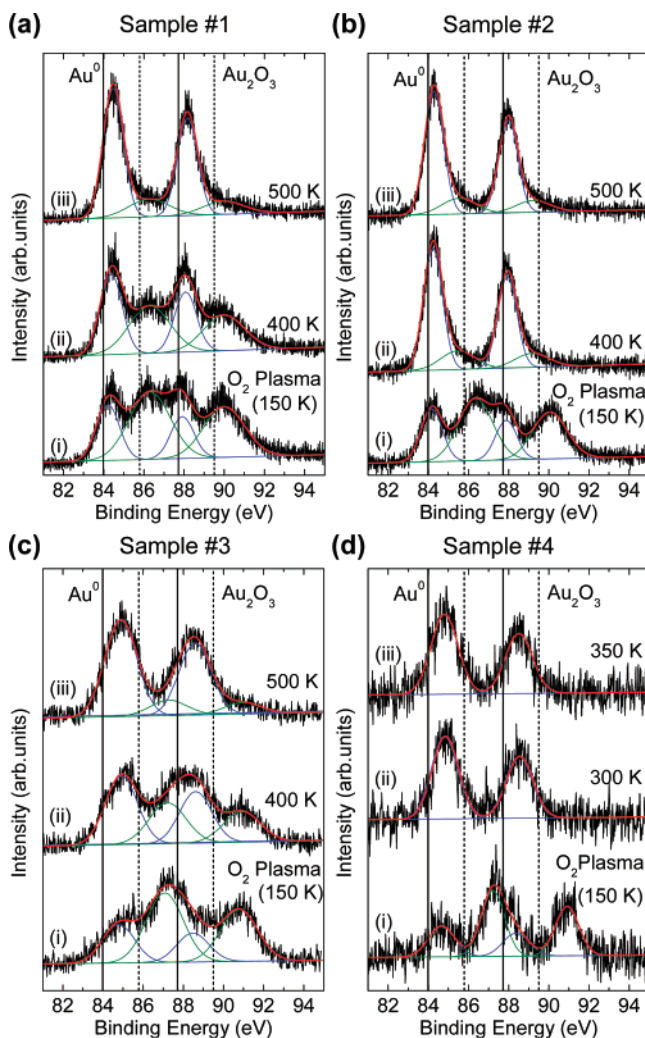
Figure 2. XPS spectra (Al Kα = 1486.6 eV) corresponding to the Au-4f core level of Au nanoparticles with two different average sizes: (a and b) ∼5 nm and (c and d) ∼1.5 nm supported on SiO₂ (a and c) and TiO₂ (b and d). The temperature-dependent spectra shown follow the decomposition of Au oxide after UHV annealing from 200 up to 500 K (10 min).

commonly attributed to initial[51,52] and final state effects.[44,53] In addition, DFT calculations by Yang et al.[54] suggested that positive core-level shifts measured for Au NPs supported on MgO(001) and TiO₂(110) could be related to the presence of oxygen vacancies in the supports.

(c) Temperature Dependence of the Thermal Decomposition of Au₂O₃. *Size Effects.* It is known that the particle size affects the reduction rate of metal nanocatalysts, and two models based on geometrical and electronic effects have been proposed.[55,56] In the geometrical model, different oxygen adsorption sites are available for differently sized clusters. In the electronic model, size-dependent changes in the electronic structure of small clusters are believed to play a role in the stability of metal oxide cluster shells. For our large NPs (∼5 nm), geometrical effects should dominate, while electronic effects may also play a role in the reduction of our small clusters (∼1.5 nm).

The influence of the particle size on the thermal stability of Au₂O₃ can be inferred by comparing XPS spectra taken on samples with two different particle size distributions supported on the same substrate (Figure 2a and c for Au/SiO₂ and Figure 2b and d for Au/TiO₂). In order to estimate the thickness of the gold oxide formed upon low-temperature O₂ plasma exposure, the model described by Nanda et al. and Wu et al. in refs 57
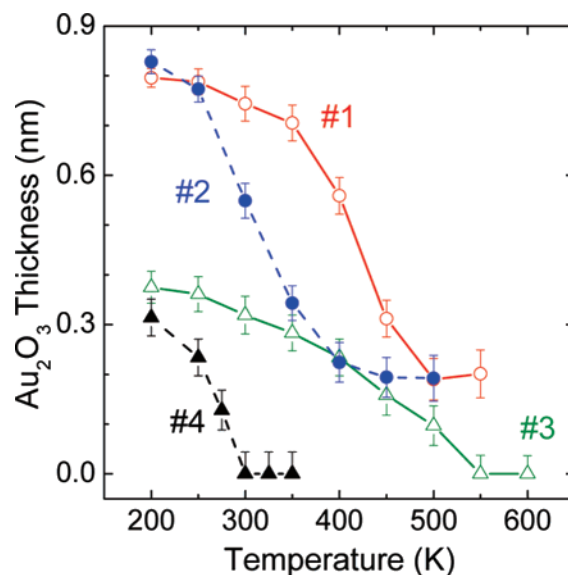

Figure 3. Temperature dependence of the decomposition of gold oxide studied for two different gold particle sizes ∼5 nm (open and closed circles) and ∼1.5 nm (open and closed triangles) supported on SiO₂ (samples 1 and 3) and TiO₂ (samples 2 and 4).

and 58 was used. Following this model, the NP shape is assumed to be spherical and composed of a metallic core (Au) and an oxidized shell (Au₂O₃). The ratio of the intensities of the photoelectron peaks (4f₇/₂ in our analysis) from the Au⁰ core and Au³⁺ shell is given by

$$\frac{I_{Au_2O_3}(\theta)}{I_{Au}(\theta)} =$$

$$\frac{K_{Au_2O_3}\int_{R_1}^{R_2}\int_0^\pi \exp\left(\dfrac{r\cos\theta - \sqrt{R_2^2 - r^2\sin^2(\theta)}}{\lambda_2}\right) r^2 \sin(\theta)\, d\theta\, dr}{K_{Au}\int_0^{R_1}\int_0^\pi \exp\left(\dfrac{r\cos\theta - \sqrt{R_2^2 - r^2\sin^2(\theta)}}{\lambda_1}\right) r^2 \sin(\theta)\, d\theta\, dr}$$

$$(1)$$

where R_1 is the radius of the NP core and R_2 is the total radius of the NP (measured by AFM). The inelastic mean free path (IMFP) of electrons in metallic Au (λ_1) is 1.781 nm.[59] Using NIST software[59] and a gold oxide density of 13.675 g/cm³ (see ref 60 for details on the structure of Au₂O₃), we estimated an IMFP (λ_2) of 1.937 nm for Au₂O₃. The constants K_{Au} and $K_{Au_2O_3}$ are related to the distinct elemental sensitivities and instrumental factors. A value of $K_{Au_2O_3}/K_{Au} = 0.32$ was used in our studies.[57] Equation 1 was evaluated numerically, and the R_1 value was varied until the $I_{Au_2O_3}(\theta)/I_{Au}(\theta)$ ratio matched the intensity ratio measured by XPS.

Figure 3 shows the calculated Au₂O₃ shell thicknesses as a function of temperature. As described above, all samples were annealed for 10 min at the respective temperatures and the XPS spectra were measured subsequently at room temperature. The maximum thicknesses of the Au₂O₃ shell formed on the large NPs deposited on SiO₂ (sample no. 1) and TiO₂ (sample no. 2) after O₂ plasma were 0.79 ± 0.02 nm and 0.83 ± 0.02 nm, respectively. For the small clusters, the initial maximum Au₂O₃ thicknesses were 0.38 ± 0.02 nm (sample no. 3, SiO₂) and 0.31 ± 0.01 nm (sample no. 4, TiO₂). For NPs deposited on both substrates, a clear size-dependence of the stability of Au₂O₃ can be inferred from Figure 3.

For the Au/TiO₂ system, the Au oxide shell was found to be more stable on the large NPs (sample no. 2), with a 50%

decomposition of the Au$_2$O$_3$ shell obtained at ~310 K as compared to ~265 K for the smaller clusters (sample no. 4). The higher surface/volume ratio present in the small clusters should contribute to their faster reduction. Nearly complete disappearance of the Au^{3+} signal (<14% of the initial Au$_2$O$_3$ thickness remaining) was observed at 300 K for the small clusters on TiO$_2$ (sample no. 4), while a substantial Au^{3+} signal (~66% of the initial Au$_2$O$_3$ thickness) could still be detected on the surface of the large clusters (sample no. 2) at 300 K and ~25% Au^{3+} signal at 500 K. A similar size-dependent trend was observed by our group during the reduction of surface Pt-oxides (PtO and PtO$_2$) on Pt NPs supported on anatase TiO$_2$ powders.[61] These results are also in agreement with data obtained by Suhonen et al.[62] on oxidized Rh clusters supported on different oxide powders, where faster reduction rates were measured for smaller clusters.

For the Au/SiO$_2$ system, the Au$_2$O$_3$ shell on smaller NPs displayed a slightly higher thermal stability at low temperature than the large NPs, with a 50% decay in the Au^{3+} signal on small clusters (sample no. 3) at 430 K as compared to a similar decay at 410 K for the large clusters (sample no. 1). On this system, a nearly complete decomposition of the Au$_2$O$_3$ shell (within the experimental error margin) was observed for the small clusters after 10 min annealing at 550 K (sample no. 3), while a ~0.2 nm-thick gold oxide layer was still present at that temperature on the large clusters (sample no. 1). The dramatic differences in the stability of Au$_2$O$_3$ on small NPs deposited on SiO$_2$ and TiO$_2$ will be discussed in the next section, where the role of the cluster support will be considered.

It is noteworthy that on both substrates only a partial reduction of the Au$_2$O$_3$ layer is observed for our large NPs (samples 1 and 2) up to an annealing temperature of ~550 K (10 min), where a ~0.2-nm-thick Au$_2$O$_3$ shell remains on both SiO$_2$ and on TiO$_2$. Further annealing (>600 K, not shown) resulted in a slow decomposition of this oxide component. However, for the smaller NPs supported on both substrates, complete Au^{3+} reduction is observed below 550 K, Figure 3. This difference can be attributed to the presence of more than one gold oxide species (surface and subsurface oxide) in these NPs and to a distinct thermal stability of such species. This is discussed in more detail in Section e. For bulk systems, typical values for the decomposition temperature of gold oxide Au$_2$O$_3$[49,60] are in the range of 360−450 K. However, the existence of a more stable form of gold oxide on Au(111), stable up to 1073 K, has also been reported by Chesters et al.[63]

Support Effects. In addition to size effects, the influence of the oxide support on the decomposition of surface oxides on metal nanoparticles cannot be neglected. As an example, Schalow et al.[14] attributed the more facile reduction of preoxidized, small (<3 nm) Pd NPs supported on Fe$_3$O$_4$/Pt(111) as compared to larger clusters (10−100 nm) because of the stronger metal−support interactions expected for small clusters.

In the current study, a drastic difference in the stability of Au$_2$O$_3$ over NPs with similar size distributions but deposited on different substrates was observed. As an example, the Au$_2$O$_3$ thicknesses obtained from the analysis of Figure 2a(ii) and 2b-(ii) (large particles, ~5 nm height) after annealing at 400 K for 10 min were 0.56 ± 0.04 nm for Au/SiO$_2$ and 0.22 ± 0.04 nm for Au/TiO$_2$. Similarly, after annealing the small NPs (~1.5 nm) at 350 K for 10 min, gold oxide shells with thicknesses of 0.28 ± 0.04 nm for Au/SiO$_2$ (not shown) and 0.0 ± 0.04 for Au/TiO$_2$ [Figure 2d(iii)] were obtained. As can be seen in Figure 3, for both particle sizes, Au$_2$O$_3$ is more easily decomposed (at lower temperature) when the NPs are supported on reducible

TiO$_2$ substrates. A tentative explanation for this distinct behavior involves oxygen spillover from the oxidized Au NP shell to the TiO$_2$/Ti substrate. This model is based on the well-known facile reduction of the TiO$_2$ support at low temperature. Oxygen vacancies created in the TiO$_2$ upon sample annealing might be replenished by oxygen from the gold oxide NP shell. Such a mechanism is not possible in the case of SiO$_2$ because it only becomes reduced well above the temperatures employed here (maximum annealing temperature of 600 K). Oxygen vacancies in the support are known to be favorable sites for strong interactions with Au NPs,[8,64,65] becoming preferential sites for the nucleation of metal clusters.[66] Furthermore, a stronger binding of Au clusters to reduced TiO$_x$ films as compared to bulk TiO$_2$ has been measured,[67] and charge-transfer phenomena from oxygen vacancies in the reduced TiO$_2$ supports to metal clusters have been discussed.[18,68] In our studies, it appears that a strong metal−support interaction for the Au/TiO$_2$ system could be responsible for the decomposition of gold oxide on TiO$_2$ at a lower temperature than that on SiO$_2$.

Interestingly, Chang et al.[69] observed that the thermal decomposition of Ta$_2$O$_5$ was faster when it was deposited directly on Ti as compared to structures where an intermediate oxygen diffusion barrier (TiN) was present (Ta$_2$O$_5$/TiN/Ti). They concluded that oxygen diffuses from the Ta$_2$O$_5$ film to the underlying Ti layers and that the Ti contributes to its reduction. Furthermore, when the Ta$_2$O$_5$ film was in direct contact with Si, no enhanced reduction was detected. Finally, it should be noted that the influence of a reducible support on oxide decomposition depends on the relative stability of the oxides involved. For example, there are reports indicating a slower decomposition rate of RhO$_x$ clusters when deposited on partially reduced Ce−Zr powders.[62] Here, the reducible oxide support is believed to act as a local *supplier* of oxygen, slowing down the metal oxide decomposition. This is, however, a different experimental system because, contrary to the case of Au on TiO$_2$, where the enthalpy of formation of Au$_2$O$_3$ is very high, Rh forms a much more stable oxide.

Because the size-dependent Au$_2$O$_3$ decomposition behavior is different for similarly sized Au clusters deposited on our two different substrates, a distinct underlying mechanism is expected. Assuming that oxygen vacancies in the oxide support play a role in the stability of the Au oxide in the Au/TiO$_2$ system, the higher stability of Au$_2$O$_3$ in large Au NPs (sample no. 2) as compared to smaller NPs (sample no. 4) could indicate that a rate-limiting step for the decomposition of Au$_2$O$_3$ is the diffusion of atomic oxygen to the Au/TiO$_2$ interface. Following this model, larger diffusion barriers to the NP/support interface must be present in the case of large Au clusters.

A schematic summary of the mechanisms proposed here for the decomposition of the Au oxide shell, formed on size-selected Au NPs supported on SiO$_2$ and TiO$_2$ upon atomic oxygen exposure, is given in Figure 4. In the SiO$_2$ case, desorption of atomic (labeled as process 1) and molecular oxygen (upon recombination, process 2) from the oxide shell are depicted. Furthermore, for the large NPs, the diffusion of subsurface oxygen to the NP surface is also considered (3). On TiO$_2$, one additional decomposition pathway (4) is proposed, where O vacancies created in the TiO$_2$ substrate during annealing are continually replenished by oxygen atom spillover from the Au oxide NP shell.

In order to demonstrate that a relatively large number of oxygen vacancies were present in our TiO$_2$ support after annealing at low temperature, we have conducted in situ XPS studies on the uncoated TiO$_2$ support after O$_2$ plasma exposure
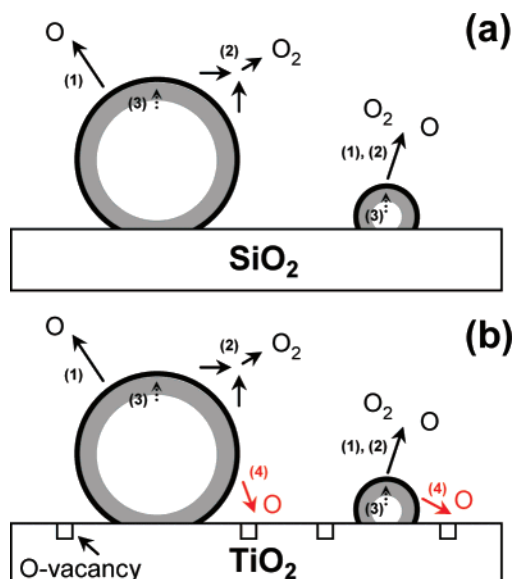
Figure 4. Schematic model illustrating different mechanisms for Au_2O_3 decomposition on large and small NPs supported on SiO_2 and TiO_2. Four processes are depicted: (1) direct desorption of atomic oxygen, (2) recombination of atomic oxygen and desorption as molecular oxygen, (3) segregation of subsurface oxygen to the NP's surface, and (4) atomic oxygen from the NP shell spills over to the TiO_2 substrate and replenishes oxygen vacancies created on TiO_2 upon sample annealing.

and subsequent thermal treatments (200−500 K) in UHV. Figure 5 displays XPS spectra of the Ti-2p region of our thin TiO_2 substrate [TiO_2(6 nm)/Ti(9 nm)/Si(111)]. The first XPS peak at 454.2 eV is assigned to Ti^0 ($2p_{3/2}$ orbital) from the underlying supporting metal film. The main doublet (459.1 ± 0.3 eV, 464.9 ± 0.3 eV) is assigned to TiO_2. The small positive BE shifts observed for the TiO_2 peaks with increasing temperature may be attributed to morphological and electronic changes in our polycrystalline substrate.[70] Although a small Ti^{3+} component is present even directly after O_2 plasma, its contribution to the overall spectral area was found to increase significantly with increasing annealing temperature, indicating the creation of additional O vacancies. Annealing to 500 K resulted in a strong increase of the Ti^{3+}/Ti^{4+} ratio (0.85 concentration ratio obtained from the area of the Ti^{3+}/Ti^{4+}-$2p_{3/2}$ peaks). At this temperature, Ti^{2+} species were also detected (6.8%). These results are in qualitative agreement with data obtained by Mizuno et al.[71] on a TiO_2 single crystal annealed at 453 K for 24 h, showing a convoluted Ti-2p spectrum with TiO_2, TiO, Ti_2O_3, and Ti_3O_5 compounds. In our case, because of the smaller thickness of our TiO_2 support, TiO_2 reduction is faster and begins at a lower temperature. Although the presence of partially reduced TiO_2 in these samples provides support for the model proposed in Figure 4b, further experimental and theoretical investigations are required to determine the role of oxygen vacancies in the thermal decomposition of Au_2O_3 in Au NPs supported on TiO_2.

(d) Time Dependence of the Thermal Decomposition of Au_2O_3. Figure 6 shows Au-4f XPS spectra from the four samples described in Table 1 measured at RT after annealing at 350 K during different time intervals (from 1 min to ~2000 min). For reference purposes, the XPS spectra measured on each sample directly after O_2 plasma exposure at 150 K are also displayed (Figure 6, curves i). Except for sample no. 4 (~1.4 nm Au particles supported on TiO_2), where a fast decomposition was observed, a gradual reduction of Au^{3+} to Au^0 is observed by XPS with increasing annealing time.
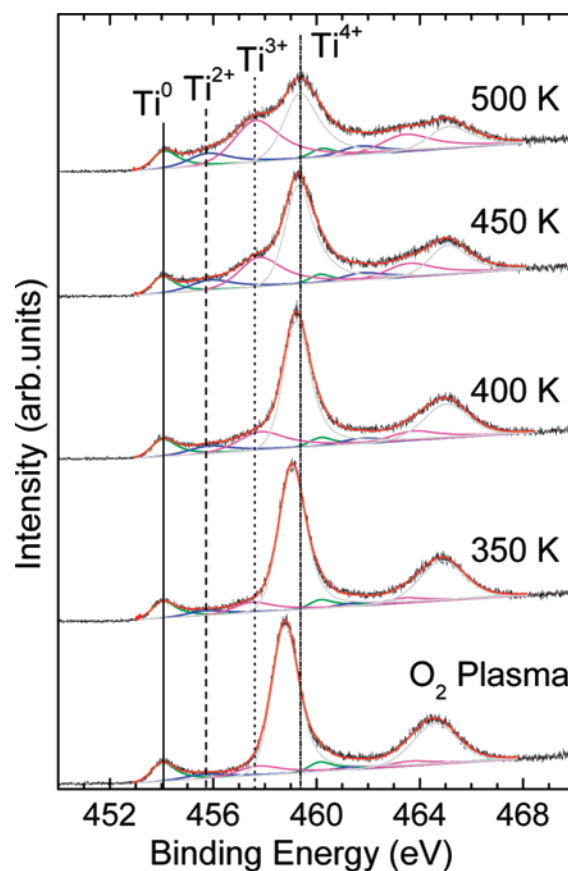

Figure 5. XPS spectra (Al Kα = 1486.6 eV) corresponding to the Ti-2p core level of a gold-free TiO_2 substrate. Chemical composition changes on Ti−O compounds were monitored after different annealing treatments at different temperatures in UHV for 10 min. The raw data were deconvoluted with Ti^0, Ti^{2+}, Ti^{3+}, and Ti^{4+} fitting components. Reference lines for the Ti-$2p_{3/2}$ XPS peak of the different Ti species are indicated.

Figure 7 shows how the thickness of the Au_2O_3 shell (Au^{3+} XPS signal) decreases as a function of annealing time for the following temperatures: 350, 375, and 400 K. The data in Figure 7 were obtained from the analysis of XPS spectra similar to the ones displayed in Figure 6 using eq 1. This study has been carried out only on samples 1, 2, and 3 (Figures 7a, b, and c, respectively). The Au^{3+} reduction in sample no. 4 (small particles on TiO_2) was so fast that a meaningful dataset could not be obtained using this procedure because the decomposition occurred in a time interval on the order of our experimental time error. This experimental error is related to the time required to increase and decrease the sample temperature from RT to the desired annealing value and back to RT for XPS analysis.

The data in Figure 7 show that the oxide decomposition slows down as the oxide shell thickness decreases (note the logarithmic time axis). Tsai et al.[37] conducted a similar study on an Au film (100 nm thick) exposed to an O_2 plasma treatment (for 1 min) based on resistance measurements performed in air (45% moisture content) at temperatures of 295, 323, 348, and 400 K. The authors discussed that the decomposition of surface Au_2O_3 in air followed first-order rate kinetics with an activation energy of 57 kJ/mol (~0.59 eV). In contrast, the XPS results in Figure 7 cannot be fitted with simple rate equations for several reasons: (i) more than one gold oxide species is present in our samples (chemisorbed O_2, surface oxide, subsurface oxide), (ii) the nanoparticle size affects the stability of each of these species, (iii) the nature of the oxide support affects the decomposition
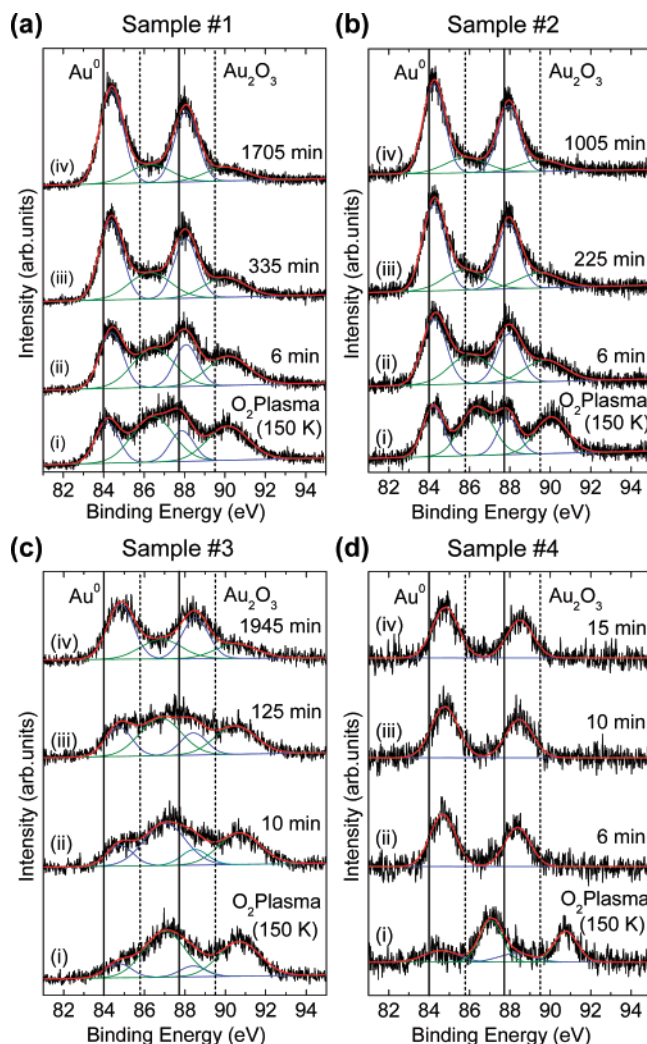
Figure 6. XPS spectra (Al Kα = 1486.6 eV) corresponding to the Au-4f core level of samples with two different average Au nanoparticle sizes: (a and b) ∼5 nm and (c and d) ∼1.5 nm supported on SiO_2 (a and c) and TiO_2 (b and d). All data were acquired after isothermal sample annealing in UHV at 350 K for different time intervals. For reference, XPS spectra measured directly after O_2 plasma exposure are also shown.

kinetics (Au/TiO₂). In the following, we discuss the curves in Figure 7 in more detail.

Support Effects. For samples with identical size distributions (samples 3 and 4, ∼1.5 nm), a faster Au^{3+} decomposition rate was observed for the NPs supported on TiO_2 (sample no. 4), Figure 6d as compared to NPs on SiO_2 (sample no. 3), Figures 6c and 7c. Although less drastic, the same observation was made for the samples containing the larger NPs (∼5 nm, sample no. 2), Figures 6a and 7a (SiO_2) and 6b and 7b (TiO_2). We attribute this effect to the strong metal−support interaction characteristic of the Au/TiO₂ system as also discussed in the temperature-dependent studies described above. Furthermore, our results indicate that such interactions affect small clusters more significantly than larger particles.[14]

Size Effects. According to previous literature,[72] the initial thickness of the Au_2O_3 shell formed on each sample should be taken into consideration in order to understand the kinetics of the thermal decomposition of oxides. Sayan et al.[72] investigated the decomposition of HfO_2 deposited on SiO_2/Si and found a nearly linear relationship between the HfO_2 thickness and the decomposition time. Furthermore, they observed that the thick-
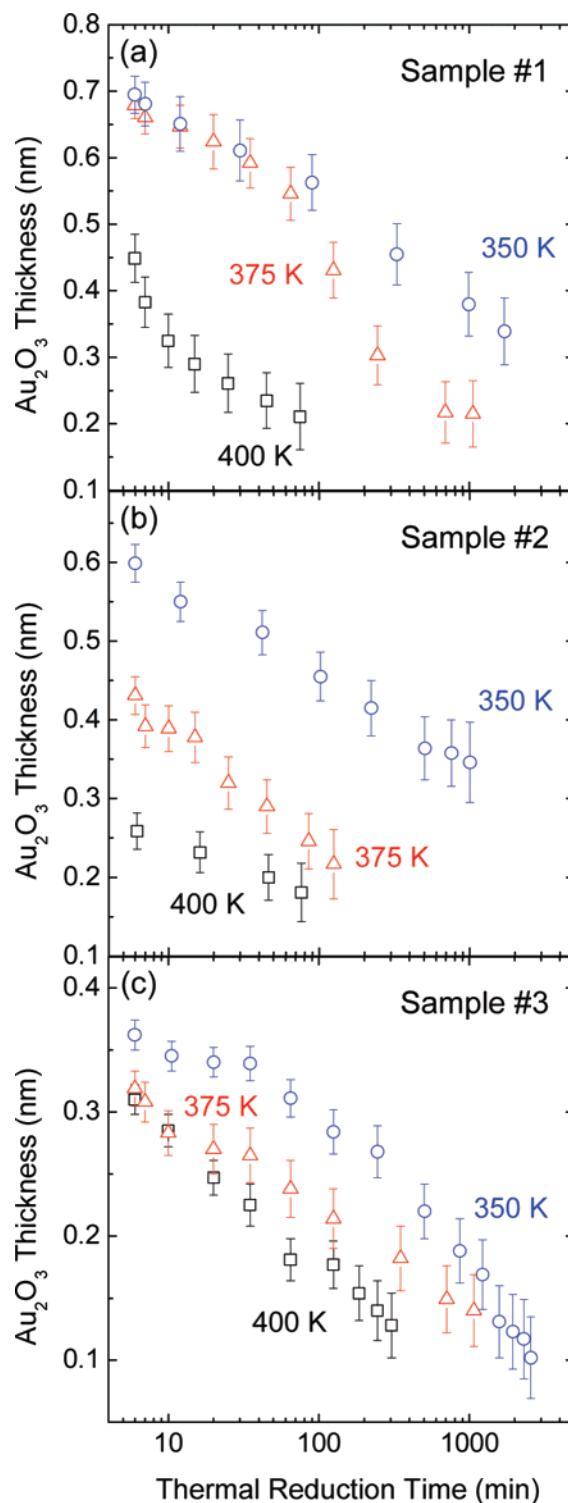

Figure 7. Time dependence of the decomposition of Au_2O_3 obtained from the XPS spectra shown in Figure 6 for three different samples: (a) sample no. 1 (Au/SiO₂, 4.9 nm), (b) sample no. 2 (Au/TiO₂, 5.4 nm), and (c) sample no. 3 (Au/SiO₂, 1.7 nm). The temperatures during isothermal annealing are indicated.

ness of the SiO_2 support did not affect the stability of HfO_2. In our experiments, thicker Au_2O_3 films were formed on the larger clusters (i.e., 0.8 ± 0.1 nm and 0.3 ± 0.1 nm for ∼5 nm and ∼1.5 nm Au NPs on TiO₂, respectively), where slower Au^{3+} decomposition rates were measured. An exception is the Au/SiO₂ system, where Au_2O_3 seems to be slightly more stable on small NPs below 550 K. As mentioned above, geometric (stronger oxygen adsorption sites on small clusters) and

electronic effects can influence the decomposition behavior on such small clusters.

In order to explain the complex kinetics of Au_2O_3 decomposition on differently sized Au NPs exclusively based on size effects, two different models can be considered: (i) the formation of an intermediate gold oxide compound[73] (e.g., Au^{3+} decomposition to Au^+) and (ii) the presence of subsurface oxygen. Although literature reports that favor each of these options exist, and both models are described below, our experimental evidence supports the presence of subsurface oxide.

The presence of Au^+ species was suggested by Pireaux et al.[49] after monitoring the decomposition of gold oxide on Au-(111) in UHV by XPS. The authors obtained atomic Au/O ratios of ~0.6 right after oxidation and ~1.4 after annealing to 340 K and concluded that Au_2O_3 (auric oxide, Au^{3+}) is formed immediately after atomic oxygen exposure, whereas the reduction process at 340 K resulted in Au_2O (aurous oxide, Au^+). However, recent DFT calculations on the stability of different gold oxides indicate that Au_2O_3 is more stable than Au_2O.[60]

Whether subsurface oxygen is present in gold films and particles upon exposure to atomic oxygen is still a matter of controversy. Lim et al.[74] used XPS to investigate the oxidation of Au NPs with different sizes supported on HOPG. Upon exposing large NPs (~7 nm) to atomic oxygen, a single peak of O-1s at 530 eV was recorded. Subsequent sample exposure to CO (3000 L) at RT resulted in the reduction of the particles. However, for smaller NPs (~3 nm), two different oxidation states (530 and 532 eV) were observed in the O-1s core level. When these particles were exposed to CO, the intensity of the O-1s peak at 530 eV was reduced significantly, whereas the peak at 532 eV was not modified. The authors attributed the second state to subsurface oxygen. The formation of subsurface oxygen was also suggested by Kim et al.[40] for small Au NPs supported on TiO_2(110). Subsurface oxygen (bulk oxide) species have also been identified on Au(111) by Min et al.,[42] and their relative stability was found to depend on the sample temperature during atomic oxygen exposure (ozone) as well as on the oxygen coverage. In fact, surface and subsurface gold oxide species as well as chemisorbed oxygen were found in bulk systems exposed to atomic oxygen at low temperature (200 K), whereas at high-temperature (400 K), only surface gold oxide species were observed. Following the findings by Min et al.,[42] a reason for the discrepancies found in the previous literature reports might be the different procedures used to deposit atomic oxygen on gold surfaces (coverage and sample temperature).

(e) Stability of Gold Oxide upon CO Dosing: Surface versus Subsurface Oxide. In order to gain insight into whether surface and subsurface gold oxide species coexist in our preoxidized size-selected Au nanoparticles supported on SiO_2 and TiO_2, we dosed the samples with CO and monitored the decomposition of gold oxide species by XPS. Figure 8 shows XPS spectra from the Au-4f core level region of our four samples (see Table 1 for details) after O_2-plasma at 150 K (i) and after subsequent 4500 L (ii) and 9000 L (iii) CO dosing at room temperature (samples 1, 2, and 3) and at 200 K (sample no. 4). Because the gold oxide compounds formed on sample no. 4 were found to decompose thermally upon annealing at RT, in order to separate gas from thermally induced decomposition of gold oxide, the CO dosing on sample no. 4 was done at 200 K.

In Figure 8a [sample no. 1, Au(~5 nm)/SiO_2], it can be seen that the relative Au^{3+} contribution to the XPS spectra decreases upon CO dosing (ii) because of Au_2O_3 decomposition as a result of CO_2 formation. Note, however, that the Au^{3+} signal does
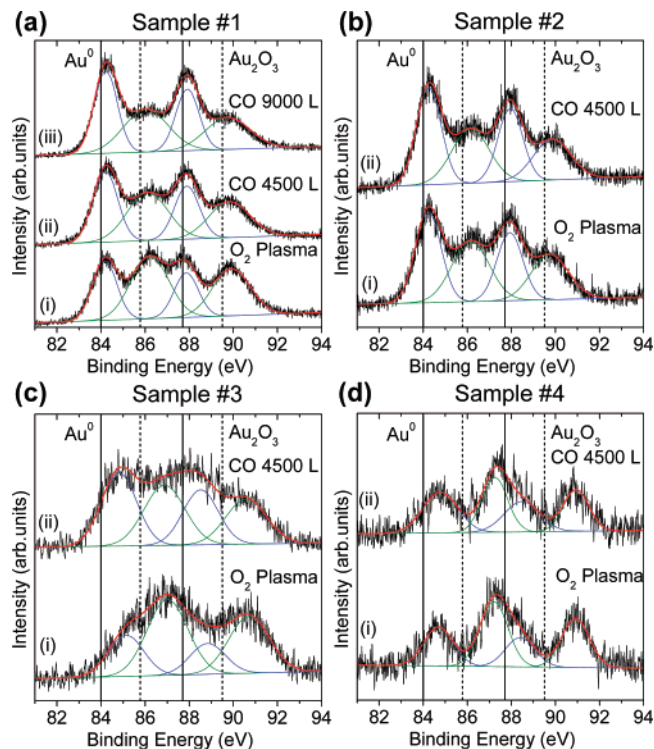

Figure 8. XPS spectra (Al Kα = 1486.6 eV) corresponding to the Au-4f core level of samples with two different average Au nanoparticle sizes: (a and b) ~5 nm and (c and d) ~1.5 nm supported on SiO_2 (a and c) and TiO_2 (b and d). The spectra shown in a−c were measured at RT after low temperature (150 K) O_2 plasma exposure ($P_{O_2} = 5.5 \times 10^{-5}$ mbar, 100 min) (i), and after subsequent CO dosing at RT (ii) 4500 L, and (iii) 9000 L. The same O_2 plasma conditions were used in d (sample no. 4), but the CO dosing was conducted at ~150 K and the XPS spectra was acquired at ~200 K.

not disappear completely, even after a 9000 L CO exposure (iii), suggesting that subsurface Au-oxide species are present. For sample no. 1, the intensity ratio of the Au^{3+}/Au^0 $4f_{7/2}$ core levels is 1.05 ± 0.04 after O_2 plasma (i), 0.68 ± 0.03 after 4500 L CO dosing (ii), and 0.52 ± 0.02 after a subsequent 4500 L CO exposure (iii). As expected, the decrease in the Au^{3+} intensity is accompanied by an increase in the Au^0 XPS signal. A similar trend was observed for sample no. 2 [Au(~5 nm)/TiO_2] in Figure 8b, although the decay in the Au^{3+}/Au^0 ratio after 4500 L CO dosing was smaller (from 0.66 ± 0.04 after O_2 plasma to 0.56 ± 0.03 after CO dosing). Samples 3 [Au-(~1.5 nm)/SiO_2] and 4 [Au(~1.5 nm)/TiO_2] display Au^{3+}/Au^0 ratios of 1.8 ± 0.3 and 1.7 ± 0.2 immediately after O exposure (i) and 1.0 ± 0.2 and 1.4 ± 0.3 after CO exposure (ii), respectively. Because CO is only expected to react with weakly bound oxygen species and surface gold oxide,[42,74] the residual Au^{3+} signal measured for all samples after high CO dosing indicates that subsurface oxygen is present in all samples.

Recent DFT calculations by Shi and Stampfl[75] on O/Au(111) revealed that the most energetically favorable configuration is an ultrathin surface-oxide-like structure (~0.31 ML oxygen coverage) with O atoms quasi-threefold coordinated to Au, and gold atoms at the surface twofold linearly coordinated to O. This structure was found to be significantly more stable (up to 420 K at atmospheric pressure and up to 200 K under ultrahigh vacuum conditions) than on-surface chemisorbed oxygen or atomically adsorbed oxygen. Furthermore, for higher oxygen coverages (>0.5 ML, as is our case), mixed on-surface + subsurface structures were found to be more favorable than pure on-surface adsorption.
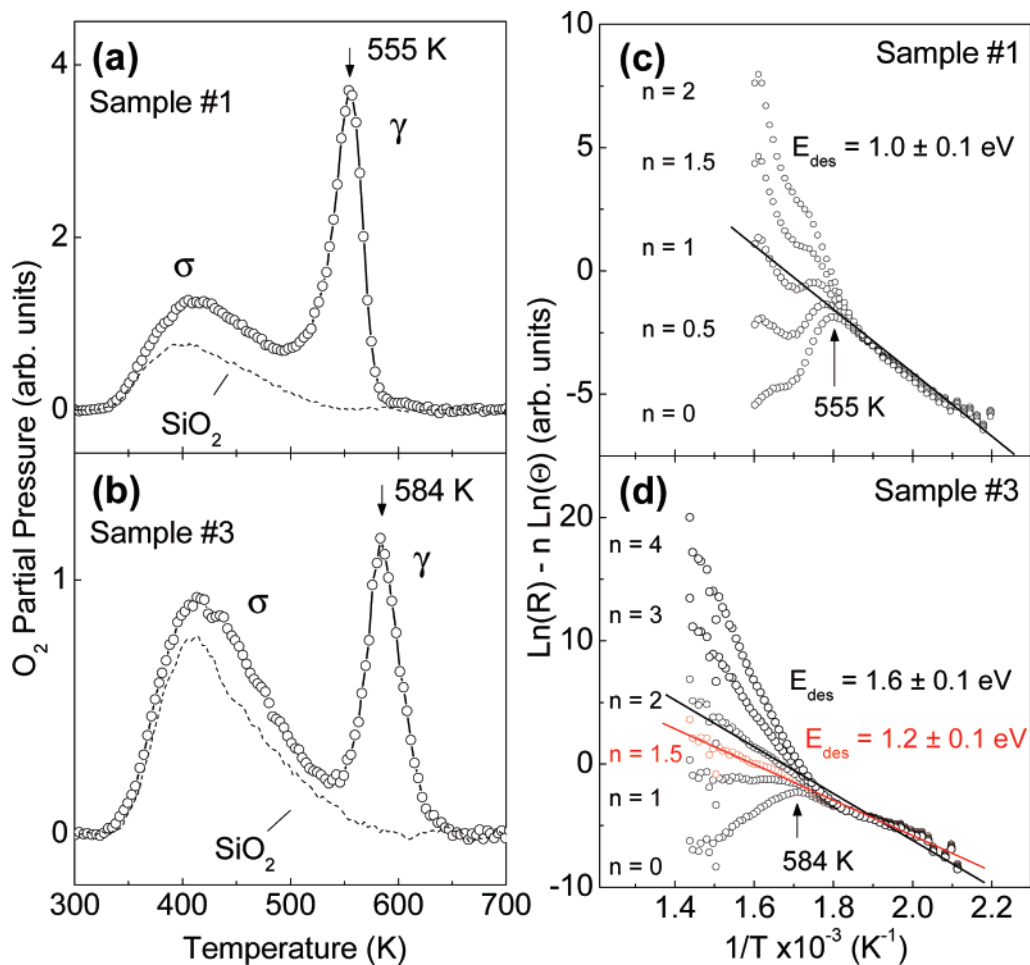
Figure 9. O_2 TPD spectra (open circles) from samples 1 (a) and 3 (b) after an *in-situ* O_2 plasma treatment at room temperature (2.3×10^{-5} mbar for 15 min). A linear heating ramp with $\beta = 5$ K/s has been used. The data obtained on a gold-free SiO_2 substrate subjected to an identical O_2 plasma treatment are also displayed for reference (dashed line). The arrows indicate the temperatures corresponding to peak maxima for O_2 desorption. Plots of $[\ln(d\theta/dt) - n \ln \theta]$ vs $1/T$ are shown for several choices of desorption kinetic order "n" for two average particle sizes of Au nanoparticles deposited on SiO_2: (c) ~5 nm and (d) ~1.5 nm.

(f) Size-Dependent O_2 Desorption (TPD). The size-dependent differences in the reduction of Au−O compounds, formed upon room temperature atomic oxygen exposure, were studied by TPD. Figure 9a and b shows O_2 desorption signals (open circles) measured on (a) sample no. 1 (Au/SiO₂, 4.9 nm) and (b) sample no. 3 (Au/SiO₂, 1.7 nm) after an O_2 plasma treatment ($P_{O_2} = 2.3 \times 10^{-5}$ mbar for 15 min). The dashed lines display control experiments conducted on gold-free SiO_2 substrates exposed to analogous O_2 plasma treatments.

Two major differences between our XPS and TPD investigations should be noted. First, the XPS samples were exposed to atomic oxygen at 150 K, while the TPD samples were dosed with O at 300 K (in order to minimize the residual gas background). According to previous studies,[42] after such RT plasma treatment the formation of bulk gold oxide is not favorable, and the TPD features described below should be attributed mainly to the desorption of chemisorbed oxygen and the decomposition of surface Au₂O₃. Second, while the TPD samples were subjected to a fast annealing cycle (80 s), the XPS samples were successively annealed from 300 to 600 K maintaining the sample temperature fixed for 10 min at 350, 400, 450, 500, 550, and 600 K, Figure 3.

A desorption peak at 401 K (σ state) was observed for the SiO_2 substrate, Figure 9a and b. Oxidized Au NPs on SiO_2 showed two characteristic desorption peaks: one at ~404 K (σ state from the substrate), and another (γ state) at ~555 K for

sample no. 1 (~5 nm Au clusters) and ~584 K for sample no. 3 (~1.5 nm Au clusters). Our TPD data indicate a size-dependent O_2 desorption in which smaller NPs show higher desorption temperatures (γ state). As expected, this size dependence is observed only for the γ state because the σ state was assigned to O_2 desorption from the substrate and the same SiO_2 support was used for both samples. This is in agreement with previous O_2 TPD desorption studies conducted by Bondzie et al.[76] on Au evaporated on TiO₂(110). They observed higher desorption temperatures (645 K) for smaller Au NPs (~0.35 ML Au coverage) as compared to larger Au NPs (520−545 K) (>6 ML Au).

In order to obtain the reaction order for O_2 desorption, we employed the method described by Saliba et al. in ref 77. Figure 9c and d shows plots of $[\ln(d\theta/dt) - n \ln \theta]$ versus $1/T$ for samples 1 and 3 after O_2 plasma. Here, θ represents the oxygen coverage and $r = d\theta/dt$ is the desorption rate. In such a plot, a linear appearance of the desorption data indicates that the correct desorption order (n) has been selected. Furthermore, the desorption energy (E_d) can be extracted from the slope of the plot. As can be seen in Figure 9c, for the large NPs the best fit to a straight line was obtained for $n = 1$, with a desorption energy of 1.0 ± 0.1 eV. Our TPD results for large Au NPs thus resemble the oxygen desorption from oxidized bulk Au.[78] First-order kinetics was assigned to the desorption of O_2 from Au(111) and Au(110) after atomic oxygen exposure (for high

oxygen coverages) by Saliba et al.[77] and Sault et al.[79] Similar results were obtained recently by Deng et al.[78] based on O_2 TPD studies on Au(111). In the latter case, the peak temperature of O_2 desorption at 550 K was independent of oxygen coverage, and it was attributed to a pseudo-first-order reaction.

In contrast, for small NPs, Figure 9d, the best fit was tentatively given by two desorption orders: $n = 1.5$ or $n = 2$, with desorption energies of 1.2 ± 0.1 and 1.6 ± 0.1 eV, respectively. The data in Figure 9d could not be fitted by first-order desorption kinetics. Despite the good agreement of the linear fit to our data assuming $n = 1.5$, the physical meaning of an intermediate reaction order is unclear. This type of non-integer reaction order may be due to a mixture of first- and second-order processes occurring simultaneously, see, for example, the work by Suemitsu et al.[80] on the desorption of hydrogen from Si(100) surfaces. Although our samples have relatively narrow particle size distributions, a small number of large particles were observed in sample no. 3, Figure 1e. Therefore, it is possible that the "mixed" ($n = 1.5-2$) reaction order determined for sample no. 3 is due to the presence of some large particles displaying $n = 1$ kinetics (similar to the large NPs on sample no. 1), and a majority of small NPs displaying $n = 2$ kinetics. Additionally, as pointed out by Temel et al.,[81] conventional first and second-order equations constitute two very simplified models for describing reaction rates in which several important physical parameters, including the presence of different adsorption sites (steps, kinks, terraces), vacancy creation upon annealing, lateral interactions between adsorbates, and adsorbate diffusion are neglected. In our case, the situation is further complicated by metal−support interactions that appear to play a role in the Au_2O_3 decomposition as well as by the presence of two different gold oxide species.

Our findings could have important implications on the performance of real-world catalysts. First, the catalytic activity of clusters is known to depend on their oxidation state, making knowledge of the stability of oxide phases at elevated temperatures and on different substrates of great technological relevance. Second, it has also been suggested that the toxicity of certain catalytic metal clusters upon release into the environment may depend on their oxidation state. Future work will focus on the influence of the oxidation state on the catalytic activity of these size-selected nanoscale systems.

Conclusions

Thermal decomposition studies on O-precovered (150 K) gold NPs supported on SiO_2 and TiO_2 have been conducted by XPS. Clear differences in the stability and decomposition kinetics of Au_2O_3 were found as a function of the average particle size and nature of the oxide support. The effect of the substrate was evidenced by a reduced stability of gold oxide on Au NPs supported on TiO_2, a system where strong metal−support interactions are expected. Here, oxygen spillover from the cluster's oxidized surface shell to O vacancies formed in the reducible TiO_2 substrate upon annealing is suggested as a possible decomposition pathway. Although both nanoparticle size and support were found to influence the stability of Au_2O_3, the support effect is more pronounced, as evidenced by a very fast reduction of Au^{3+} in Au/TiO_2, and enhanced gold oxide stability in Au/SiO_2. Furthermore, nearly complete reduction of small ($\sim$1.5 nm diameter) NPs was observed at 300 K for Au/TiO_2 and at 550 K for Au/SiO_2. In contrast, for larger clusters only partial Au_2O_3 decomposition was observed up to 600 K. This suggests that at least on the large NPs two different oxygen species are present: surface gold oxide that decomposes

at temperatures below 600 K and bulk or subsurface oxide that is stable well above 600 K. In addition, for the small clusters, the presence of surface and subsurface oxide was confirmed by CO dosing experiments. A decrease in the Au^{3+} signal and an increase in Au^0 upon CO exposure indicated the reduction of surface gold oxide. The observation of incomplete Au^{3+} reduction for CO dosings as large as 9000 L provided clear support for the presence of a stable subsurface gold oxide species in all samples. Finally, TPD data obtained after room temperature atomic oxygen exposure revealed distinct O_2 desorption temperatures on differently sized Au nanoparticles supported on SiO_2. A higher desorption temperature (584 K) was observed for $\sim$1.5 nm clusters, as compared to 555 K for $\sim$5 nm large clusters. These results indicate that the stability of gold oxide species strongly depends on the cluster size.

Supporting Information Available: Histograms of the particle height distributions and XPS spectra of the Au-4f region acquired after different X-ray exposure times. This material is available free of charge via the Internet at http://pubs.acs.org.

References and Notes

(1) Hammer, B.; Norskov, J. K. *Nature* **1995**, *376*, 238.
(2) Bond, G. C. *Catal. Today* **2002**, *72*, 5.
(3) Davis, R. J. *Science* **2003**, *301*, 926.
(4) Tanaka, K.; Tamaru, K. *J. Catal.* **1963**, *2*, 366.
(5) Haruta, M.; Kobayashi, T.; Sano, H.; Yamada, N. *Chem. Lett.* **1987**, 405.
(6) Hayashi, T.; Tanaka, K.; Haruta, M. *J. Catal.* **1998**, *178*, 566.
(7) Cho, A. *Science* **2003**, *299*, 1684.
(8) Chen, M. S.; Goodman, D. W. *Acc. Chem. Res.* **2006**, *39*, 739.
(9) Okumura, M.; Kitagawa, Y.; Haruta, M.; Yamaguchi, K. *Appl. Catal., A* **2005**, *291*, 37.
(10) Schwartz, V.; Mullins, D. R.; Yan, W. F.; Chen, B.; Dai, S.; Overbury, S. H. *J. Phys. Chem. B* **2004**, *108*, 15782.
(11) Fu, L.; Wu, N. Q.; Yang, J. H.; Qu, F.; Johnson, D. L.; Kung, M. C.; Kung, H. H.; Dravid, V. P. *J. Phys. Chem. B* **2005**, *109*, 3704.
(12) Casaletto, M. P.; Longo, A.; Martorana, A.; Prestianni, A.; Venezia, A. M. *Surf. Interface Anal.* **2006**, *38*, 215.
(13) Peuckert, M. *J. Phys. Chem.* **1985**, *89*, 2481.
(14) Schalow, T.; Brandt, B.; Starr, D. E.; Laurin, M.; Shaikhutdinov, S. K.; Schauermann, S.; Libuda, J.; Freund, H. J. *Phys. Chem. Chem. Phys.* **2007**, *9*, 1347.
(15) Minico, S.; Scire, S.; Crisafulli, C.; Visco, A. M.; Galvagno, S. *Catal. Lett.* **1997**, *47*, 273.
(16) Dekkers, M. A. P.; Lippits, M. J.; Nieuwenhuys, B. E. *Catal. Lett.* **1998**, *56*, 195.
(17) Wu, X.; Senapati, L.; Nayak, S. K.; Selloni, A.; Hajaligol, M. *J. Chem. Phys.* **2002**, *117*, 4010.
(18) Laursen, S.; Linic, S. *Phys. Rev. Lett.* **2006**, *97*, 026101.
(19) Costello, C. K.; Kung, M. C.; Oh, H. S.; Wang, Y.; Kung, H. H. *Appl. Catal., A* **2002**, *232*, 159.
(20) Guzman, J.; Gates, B. C. *J. Phys. Chem. B* **2002**, *106*, 7659.
(21) Fu, Q.; Saltsburg, H.; Flytzani-Stephanopoulos, M. *Science* **2003**, *301*, 935.
(22) Liu, Z. P.; Jenkins, S. J.; King, D. A. *Phys. Rev. Lett.* **2005**, *94*, 196102.
(23) Remediakis, I. N.; Lopez, N.; Norskov, J. K. *Appl. Catal., A* **2005**, *291*, 13.
(24) Liu, Z. P.; Hu, P.; Alavi, A. *J. Am. Chem. Soc.* **2002**, *124*, 14770.
(25) Yoon, B.; Hakkinen, H.; Landman, U. *J. Phys. Chem. A* **2003**, *107*, 4066.
(26) Wang, J. G.; Hammer, B. *Phys. Rev. Lett.* **2006**, *97*, 136107.
(27) Chretien, S.; Gordon, M. S.; Metiu, H. *J. Chem. Phys.* **2004**, *121*, 3756.
(28) Rousseau, R.; Marx, D. *J. Chem. Phys.* **2000**, *112*, 761.
(29) Okumura, M.; Kitagawa, Y.; Haruta, M.; Yamaguchi, K. *Chem. Phys. Lett.* **2001**, *346*, 163.
(30) Krozer, A.; Rodahl, M. *J. Vac. Sci. Technol., A* **1997**, *15*, 1704.
(31) Koslowski, B.; Boyen, H. G.; Wilderotter, C.; Kastle, G.; Ziemann, P.; Wahrenberg, R.; Oelhafen, P. *Surf. Sci.* **2001**, *475*, 1.

(32) Juodkazis, K.; Juodkazyte, J.; Jasulaitiene, V.; Lukinskas, A.; Sebeka, B. *Electrochem. Commun.* **2000**, *2*, 503.

(33) Canning, N. D. S.; Outka, D.; Madix, R. J. *Surf. Sci.* **1984**, *141*, 240.

(34) Irissou, E.; Denis, M. C.; Chaker, M.; Guay, D. *Thin Solid Films* **2005**, *472*, 49.

(35) Boyen, H. G.; Kastle, G.; Weigl, F.; Koslowski, B.; Dietrich, C.; Ziemann, P.; Spatz, J. P.; Riethmuller, S.; Hartmann, C.; Moller, M.; Schmid, G.; Garnier, M. G.; Oelhafen, P. *Science* **2002**, *297*, 1533.

(36) Lim, D. C.; Lopez-Salido, I.; Dietsche, R.; Bubek, M.; Kim, Y. D. *Surf. Sci.* **2006**, *600*, 507.

(37) Tsai, H. C.; Hu, E.; Perng, K.; Chen, M. K.; Wu, J. C.; Chang, Y. S. *Surf. Sci.* **2003**, *537*, L447.

(38) Deng, X. Y.; Min, B. K.; Liu, X. Y.; Friend, C. M. *J. Phys. Chem. B* **2006**, *110*, 15982.

(39) Stiehl, J. D.; Gong, J. L.; Ojifinni, R. A.; Kim, T. S.; McClure, S. M.; Mullins, C. B. *J. Phys. Chem. B* **2006**, *110*, 20337.

(40) Kim, T. S.; Stiehl, J. D.; Reeves, C. T.; Meyer, R. J.; Mullins, C. B. *J. Am. Chem. Soc.* **2003**, *125*, 2018.

(41) Gottfried, J. M.; Christmann, K. *Surf. Sci.* **2004**, *566*, 1112.

(42) Min, B. K.; Alemozafar, A. R.; Pinnaduwage, D.; Deng, X.; Friend, C. M. *J. Phys. Chem. B* **2006**, *110*, 19833.

(43) Ono, L. K.; Sudfeld, D.; Roldan Cuenya, B. *Surf. Sci.* **2006**, *600*, 5041.

(44) Roldan Cuenya, B.; Baeck, S. H.; Jaramillo, T. F.; McFarland, E. W. *J. Am. Chem. Soc.* **2003**, *125*, 12928.

(45) Kastle, G.; Boyen, H. G.; Weigl, F.; Lengl, G.; Herzog, T.; Ziemann, P.; Riethmuller, S.; Mayer, O.; Hartmann, C.; Spatz, J. P.; Moller, M.; Ozawa, M.; Banhart, F.; Garnier, M. G.; Oelhafen, P. *Adv. Funct. Mater.* **2003**, *13*, 853.

(46) Naitabdi, A.; Ono, L. K.; Roldan Cuenya, B. *Appl. Phys. Lett.* **2006**, *89*, 043101.

(47) Jaramillo, T. F.; Baeck, S. H.; Roldan Cuenya, B.; McFarland, E. W. *J. Am. Chem. Soc.* **2003**, *125*, 7148.

(48) Ono, L. K.; Roldan Cuenya, B. *Catal. Lett.* **2007**, *113*, 86.

(49) Pireaux, J. J.; Liehr, M.; Thiry, P. A.; Delrue, J. P.; Caudano, R. *Surf. Sci.* **1984**, *141*, 221.

(50) Chusuei, C. C.; Lai, X.; Luo, K.; Goodman, D. W. *Top. Catal.* **2001**, *14*, 71.

(51) Mason, M. G. *Phys. Rev. B* **1983**, *27*, 748.

(52) Zhang, P.; Sham, T. K. *Phys. Rev. Lett.* **2003**, *90*, 245502.

(53) Wertheim, G. K.; Dicenzo, S. B.; Youngquist, S. E. *Phys. Rev. Lett.* **1983**, *51*, 2310.

(54) Yang, Z. X.; Wu, R. Q. *Phys. Rev. B* **2003**, *67*, 081403.

(55) Anderson, J. R. *Adv. Catal.* **1973**, *23*, 1.

(56) Sinfelt, J. H.; Yates, D. J. C.; Carter, J. L. *J. Catal.* **1972**, *24*, 283.

(57) Nanda, J.; Kuruvilla, B. A.; Sarma, D. D. *Phys. Rev. B* **1999**, *59*, 7473.

(58) Wu, C. K.; Yin, M.; O'Brien, S.; Koberstein, J. T. *Chem. Mater.* **2006**, *18*, 6054.

(59) NIST Inelastic Mean Free Path Database, version 1.1; http://www.nist.gov/srd/nist71.htm.

(60) Shi, H.; Asahi, R.; Stampfl, C. *Phys. Rev. B* **2007**, *75*, 205125.

(61) Croy, J. R.; Mostafa, S.; Liu, J.; Sohn, Y.; Roldan Cuenya, B. *Catal. Lett.* **2007**, *118*, 1.

(62) Suhonen, S.; Hietikko, M.; Polvinen, R.; Valden, M.; Laitinen, R.; Kallinen, K.; Harkonen, M. *Surf. Interface Anal.* **2002**, *34*, 76.

(63) Chesters, M. A.; Somorjai, G. A. *Surf. Sci.* **1975**, *52*, 21.

(64) Vittadini, A.; Selloni, A. *J. Chem. Phys.* **2002**, *117*, 353.

(65) Vijay, A.; Mills, G.; Metiu, H. *J. Chem. Phys.* **2003**, *118*, 6536.

(66) Matthey, D.; Wang, J. G.; Wendt, S.; Matthiesen, J.; Schaub, R.; Laegsgaard, E.; Hammer, B.; Besenbacher, F. *Science* **2007**, *315*, 1692.

(67) Chen, M. S.; Luo, K.; Kumar, D.; Wallace, W. T.; Yi, C. W.; Gath, K. K.; Goodman, D. W. *Surf. Sci.* **2007**, *601*, 632.

(68) Molina, L. M.; Rasmussen, M. D.; Hammer, B. *J. Chem. Phys.* **2004**, *120*, 7673.

(69) Chang, J. P.; Steigerwald, M. L.; Fleming, R. M.; Opila, R. L.; Alers, G. B. *Appl. Phys. Lett.* **1999**, *74*, 3705.

(70) Kumar, D.; Chen, M. S.; Goodman, D. W. *Thin Solid Films* **2006**, *515*, 1475.

(71) Mizuno, Y.; King, F. K.; Yamauchi, Y.; Homma, T.; Tanaka, A.; Takakuwa, Y.; Momose, T. *J. Vac. Sci. Technol., A* **2002**, *20*, 1716.

(72) Sayan, S.; Garfunkel, E.; Nishimura, T.; Schulte, W. H.; Gustafsson, T.; Wilk, G. D. *J. Appl. Phys.* **2003**, *94*, 928.

(73) Kitagawa, H.; Kojima, N.; Nakajima, T. *J. Chem. Soc., Dalton Trans.* **1991**, 3121.

(74) Lim, D. C.; Lopez-Salido, I.; Dietsche, R.; Bubek, M.; Kim, Y. D. *Chem. Phys.* **2006**, *330*, 441.

(75) Shi, H.; Stampfl, C. *Phys. Rev. B* **2007**, *76*, 075327.

(76) Bondzie, V. A.; Parker, S. C.; Campbell, C. T. *Catal. Lett.* **1999**, *63*, 143.

(77) Saliba, N.; Parker, D. H.; Koel, B. E. *Surf. Sci.* **1998**, *410*, 270.

(78) Deng, X. Y.; Min, B. K.; Guloy, A.; Friend, C. M. *J. Am. Chem. Soc.* **2005**, *127*, 9267.

(79) Sault, A. G.; Madix, R. J.; Campbell, C. T. *Surf. Sci.* **1986**, *169*, 347.

(80) Suemitsu, M.; Kim, K. J.; Miyamoto, N. *Phys. Rev. B* **1994**, *49*, 11480.

(81) Temel, B.; Meskine, H.; Reuter, K.; Scheffler, M.; Metiu, H. *J. Chem. Phys.* **2007**, *126*, 204711.